# Supplementary Information: Acoustic control of Rayleigh-regime liquid-jet breakup using a through-hole MHz transducer

K. Nguyen[1], K. Ahmed[2], J. Friend[1,3*]

[1]Medically Advanced Devices Laboratory, Center for Medical Devices, Department of Mechanical and Aerospace Engineering, University of California San Diego, La Jolla, CA, 92093-0411, USA.

[2]Propulsion and Energy Research Lab, Department of Mechanical and Aerospace Engineering, University of Central Florida, Orlando, FL, 32816, USA.

[3]Medically Advanced Devices Laboratory, Department of Mechanical Engineering and Materials Science, Washington University in St. Louis, 1 Brookings Drive, St. Louis, MO, 63130, USA.

*Corresponding author(s). E-mail(s): jamesfriend@wustl.edu;

## S1 Detailed experimental methods

### S1.1 Device fabrication and acoustic characterization

The nozzle–transducer assembly was designed to place the acoustic source at the jet exit while preserving a simple through-flow geometry suitable for repeatable fluid-mechanics measurements. The assembly consisted of a through-hole thickness-mode transducer, a compact electrical connection for actuation and monitoring, and a three-dimensional printed resin housing that aligned the fluid supply with the drilled transducer opening. A 500 μm-thick, single-side-polished, 127.68° Y-rotated lithium niobate wafer with Ti/Au electrodes on both faces was diced into 10 mm × 10 mm × 0.5 mm chips. Through-holes were drilled using a 1 mm diamond drill bit mounted on a rotary tool workstation, following procedures for brittle piezoelectric substrates described previously (Shilton et al. 2011; Vasan et al. 2020). The through-holes were then measured to be 1 mm. Each transducer was bonded to a 2 cm-long stainless-steel tube with 2 mm outer diameter and 1 mm inner diameter using a low-viscosity rigid epoxy. The tube–transducer subassembly was connected to the resin housing with heat-shrink tubing. This modular design allowed damaged or inefficient transducers to be replaced without rebuilding the full fluidic fixture.

The transducer was bonded to the stainless-steel tube through a rigid epoxy layer, which introduces inherent energy loss. The layer absorbs part of the vibrational energy and attenuates both the force and velocity transmitted to the fluid, consistent with the known behavior of bonded piezoelectric assemblies (Bolstad et al. 2023). The epoxy bond-line thickness therefore determines the baseline input power required to produce a measurable effect on the jet. During fabrication, the bond line was minimized by applying the epoxy under gentle compression. Variability in bond-line thickness across hand-assembled devices was the primary source of device-to-device performance variation observed during development.

The operating frequency and voltage-to-particle-velocity calibration were determined from laser Doppler vibrometry (LDV) of the assembled transducer. The measurements were performed on the complete assembly, including the device connected to the tubing and mounted within the 3D-printed housing, without any liquid loading. The scan points were spaced 60 $\mu$m apart and arranged in three concentric rings surrounding the through-hole. The radial spacing between adjacent rings, as well as the distance between the edge of the through-hole and the innermost ring, was also 60 $\mu$m. The LDV frequency sweep

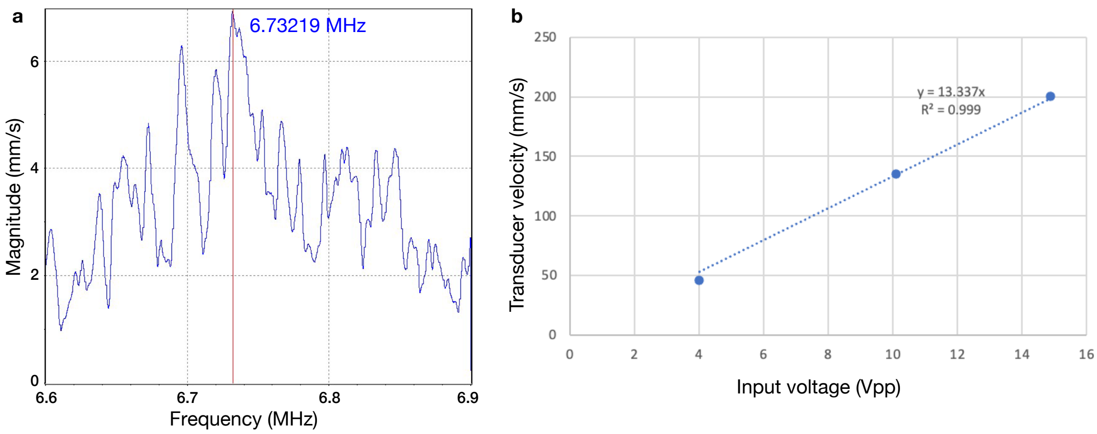


**Fig. S1** LDV characterization of the through-hole thickness-mode transducer. (a) Frequency sweep of the transducer surface particle velocity showing a response maximum at $f = 6.732$ MHz; the vertical marker indicates the selected operating frequency. (b) Calibration of particle velocity with input voltage at the selected operating frequency. The fit gives $\dot{\xi}_p = (13.337 \text{ mm s}^{-1}\text{ V}^{-1})V_{\text{pp}}$ with $R^2 = 0.999$.

showed a local maximum in the measured surface particle velocity at $f = 6.732$ MHz (Fig. S1a). The device was therefore operated at $f_d \approx 6.7$ MHz for the jet-breakup experiments. At this frequency, the measured transducer particle velocity increased approximately linearly with applied voltage over the calibration range,

$$\dot{\xi}_p = (13.337 \text{ mm s}^{-1}\text{ V}^{-1})V_{\text{pp}}, \qquad R^2 = 0.999, \tag{S1}$$

where $V_{\text{pp}}$ is the applied peak-to-peak voltage. This calibration was used to convert each applied voltage to the particle velocity $\dot{\xi}_p$ and to calculate the normalized forcing amplitude $u^* = \dot{\xi}_p/u_0$.

Complete dry and liquid-loaded impedance/admittance spectra were not available for the assembled device used in the reported measurements. Accordingly, impedance was not used as a quantitative input to the data analysis. The resonance selection and forcing calibration were based on the LDV measurements in Fig. S1, while electrical input power was estimated at the operating condition from the simultaneously measured voltage and current waveforms.

## S1.2 Flow delivery, imaging, and electrical characterization

Flow was supplied by a syringe pump, while the delivered mass flow rate was independently checked using a balance. Before each recording, the system was allowed to run for 5 s after changing the flow or acoustic condition so that the observed jet state corresponded to steady operation. The jet was backlit with a diffuse LED source and recorded using a high-speed camera at 50 000 fps. Images were collected with a macro lens. Various sinusoidal signals at the device resonance were generated using a signal generator, amplified, and sent to the transducer. True power inputs were computed from measured voltage and current using voltage and current probes connected to a digital oscilloscope.

Because nozzle exit geometry can significantly influence jet morphology and breakup behavior (McCarthy and Molloy 1974), all primary experiments were conducted using a single nozzle–transducer assembly to ensure geometric consistency across flow rate, fluid viscosity, and actuation amplitude. Experiments performed on additional devices exhibited qualitatively similar trends, confirming that the observed phenomena are not artifacts of a particular device, although absolute breakup lengths varied with device efficiency. A single-device protocol was therefore adopted as the most controlled approach for the hand-fabricated nozzle.

The experimental parameter space is characterized using the Weber number, Ohnesorge number, and Reynolds number,

$$\text{We} = \frac{\rho u_0^2 d}{\sigma}, \qquad \text{Oh} = \frac{\mu}{\sqrt{\rho\sigma d}}, \qquad \text{Re} = \frac{\rho u_0 d}{\mu}, \tag{S2}$$

where $u_0$ is the mean jet velocity at the nozzle exit, $d$ is the nozzle diameter, $\rho$ is the fluid density, $\sigma$ is the surface tension, and $\mu$ is the dynamic viscosity. Breakup length is reported in normalized form as $L_b/d$. The acoustic forcing amplitude is characterized by the ratio $u^* = \dot{\xi}_p/u_0$, where $\dot{\xi}_p$ is the transducer surface particle velocity measured by laser Doppler vibrometry at the device resonance. This ratio compares the imposed acoustic motion with the convective velocity of the jet and is more physically meaningful than electrical driving voltage alone. Fluid properties and dimensionless groups are compiled in Table S1, and a complete condition-log template is provided as a .csv file, available at doi:10.6075/J02N52F5.

**Table S1** Physical properties of the test fluids at 20 °C, corresponding Ohnesorge number $\mathrm{Oh} = \mu/\sqrt{\rho\sigma d}$, and dimensionless flow parameters $\mathrm{We} = \rho u_0^2 d/\sigma$ and $\mathrm{Re} = \rho u_0 d/\mu$ for each flow rate tested. Here $d = 1\,\mathrm{mm}$ is the nozzle inner diameter, $u_0$ is the mean jet velocity at the nozzle exit, and G/W denotes glycerol–water solution. Fluid-property data are from Takamura et al. (2012).

| Fluid | $\rho$ (kg m$^{-3}$) | $\mu$ (mPa s) | $\sigma$ (mN m$^{-1}$) | Oh | $Q$ (mL min$^{-1}$) | Re | We |
|---|---|---|---|---|---|---|---|
| DI water | 998 | 1.04 | 73.2 | 0.0038 | 30 | 611 | 5.5 |
| | | | | | 40 | 815 | 9.8 |
| | | | | | 50 | 1018 | 15.3 |
| | | | | | 60 | 1222 | 22.1 |
| | | | | | 70 | 1425 | 30.1 |
| | | | | | 80 | 1629 | 39.3 |
| | | | | | 90 | 1833 | 49.7 |
| 20/80 wt% G/W | 1047 | 1.84 | 71.7 | 0.0067 | 30 | 362 | 5.9 |
| 40/60 wt% G/W | 1100 | 3.63 | 70.0 | 0.0131 | 30 | 193 | 6.4 |
| 60/40 wt% G/W | 1156 | 11.67 | 68.5 | 0.0415 | 30 | 63 | 6.8 |

## S1.3 Breakup-length image analysis

The breakup length of a liquid jet is commonly associated with the intact length: the distance from the nozzle over which the jet remains continuously connected before the first liquid disconnection (Eggers and Villermaux 2008). Because this distance fluctuates in time, the breakup length should be treated as a statistical quantity rather than determined from a single image or a single breakup event. In the present experiments, high-speed imaging captured the full steady-state breakup process over many repeated breakup events. We therefore distinguish between the instantaneous jet length $L_j(t)$ and the reported breakup length $L_b$.

The instantaneous jet length $L_j(t)$ was defined for each frame as the shortest distance from the nozzle exit to the first liquid disconnection. In contrast, the reported breakup length $L_b$ was defined as the mean of statistically separated breakup-event minima. This distinction was necessary because directly averaging all instantaneous values of $L_j(t)$ produces a time-weighted average of a temporally correlated signal rather than an event-averaged breakup length. Multiple neighboring frames may correspond to the same breakup cycle, and treating every frame as an independent event can overrepresent correlated jet states. Averaging all frames of $L_j(t)$ can therefore produce a larger apparent breakup length and a larger apparent standard deviation than averaging only statistically separated breakup-event minima.

For each high-speed video, the image-processing routine produced a time series of instantaneous jet lengths $L_j(t_n)$, where

$$t_n = \frac{n}{f_s}, \tag{S3}$$

and $f_s$ is the camera frame rate. The temporal correlation of this signal was estimated using the normalized autocorrelation of the fluctuation signal. The mean jet length was first subtracted from the instantaneous jet-length sequence,

$$L'_j(t_n) = L_j(t_n) - \overline{L_j}, \tag{S4}$$

where $\overline{L_j}$ is the mean of the measured jet-length sequence for that video. The normalized autocorrelation was then computed for non-negative lag index $k$ as

$$\rho(k) = \frac{\sum_{n=1}^{N-k} L'_j(t_n) L'_j(t_{n+k})}{\sum_{n=1}^{N} \left[L'_j(t_n)\right]^2}, \qquad k \geq 0. \tag{S5}$$

With this normalization, $\rho(0) = 1$. The first positive lag at which $\rho(k)$ crossed zero was identified as $k_c$. The corresponding decorrelation time was calculated as

$$\tau_c = \frac{k_c}{f_s}. \tag{S6}$$

Candidate breakup events were identified as local minima in $L_j(t)$. A candidate minimum was retained only if it satisfied two criteria. First, its prominence had to exceed 30% of the full jet-length range for that video,

$$P_i > 0.30\left(L_{j,\max} - L_{j,\min}\right), \tag{S7}$$

where $P_i$ is the prominence of the $i$th candidate minimum. This criterion removed weak local fluctuations that did not correspond to clear breakup-cycle minima. Second, retained minima were required to be separated from neighboring retained minima by at least $2\tau_c$. This spacing criterion was used to avoid counting multiple temporally correlated minima from the same breakup cycle as independent breakup events.

The autocorrelation-based spacing criterion follows standard practice in experimental-flow statistics, where temporal correlation reduces the effective number of independent samples (Allen and Tildesley 1989). Sciacchitano and Wieneke (2016) showed that the effective number of independent samples is determined by the autocorrelation function, that the autocorrelation summation is commonly truncated at the first zero crossing, and that the effective sample size can be estimated from an integral time scale. For a total observation time $T$, the effective number of independent samples may be approximated as

$$N_{\text{eff}} \approx \frac{T}{2T_{\text{int}}}, \tag{S8}$$

where $T_{\text{int}}$ is the integral time scale. In the present work, $\tau_c$ is defined using the first zero crossing of the measured jet-length autocorrelation rather than the integral time scale itself. Therefore, the $2\tau_c$ spacing rule should not be interpreted as a direct consequence of the formulation above. Instead, it is used as a conservative decorrelation criterion that is consistent with autocorrelation-based effective-sample-size analysis. Benedict and Gould (1996) provide additional support for accounting for finite sampling and statistical uncertainty when estimating flow statistics from experimentally measured time series.

After filtering, the reported breakup length was calculated as the mean of the retained breakup-event minima,

$$L_b = \frac{1}{M}\sum_{i=1}^{M} L_{b,i}, \tag{S9}$$

where $M$ is the number of retained breakup events and $L_{b,i}$ is the instantaneous jet length at the $i$th retained minimum. Results are reported in dimensionless form as $L_b/d$. Error bars represent the standard deviation of the retained breakup-event lengths,

$$\sigma_{L_b} = \sqrt{\frac{1}{M-1}\sum_{i=1}^{M}\left(L_{b,i}-L_b\right)^2}, \tag{S10}$$

also normalized by $d$.

To test the sensitivity of the method to the event-selection threshold, the same jet-length time series were reprocessed using local-minimum prominence thresholds from 5% to 30%. The sensitivity was quantified as the percent change in mean breakup length relative to the default 30% threshold. Increasing the prominence threshold reduced the number of retained breakup events, as expected. However, the resulting mean breakup lengths changed by less than 5% relative to the default threshold, and the trends with acoustic forcing, Weber number, and Ohnesorge number were unchanged. This sensitivity test indicates that the observed reduction in breakup length under MHz-order acoustic excitation is not an artifact of the chosen prominence threshold.

## S1.4 Repeatability, controls, and uncertainty reporting

For compatibility with experimental fluid-mechanics reporting, the data analysis was organized around repeatable operating points rather than single representative videos. Unless stated otherwise, each plotted condition represents at least five independent recordings collected after the flow and acoustic drive had reached steady operation. Error bars in the main figures denote the standard deviation of retained event-wise breakup lengths, normalized by the nozzle diameter. This quantity reports the physical cycle-to-cycle variability of the breakup process. When the uncertainty of the mean breakup length is required, it should be calculated from the retained independent events as $\sigma_{L_b}/\sqrt{M}$ or from the independent-video means, depending on whether the intended comparison is event-level or run-level.

Several controls were used to separate acoustic forcing from geometric and wetting effects. First, all primary parametric sweeps were performed on a single nozzle–transducer assembly so that the exit geometry was fixed across flow rate, fluid viscosity, and actuation amplitude. Second, delivered flow rate was checked gravimetrically to reduce uncertainty from syringe-pump calibration. Third, the base-wetting experiment in Sec. 3.4 was used as a control for changes in the effective exit geometry and liquid–solid contact area.

**Table S2** Image-processing parameters used for droplet segmentation and filtering.

| Parameter | Value |
|---|---|
| Segmentation method | Background difference |
| Intensity threshold | 50 grayscale levels |
| Gaussian blur kernel size | 1 pixel |
| Morphological opening iterations | 0 |
| Morphological closing iterations | 1 |
| Hole filling | Enabled |
| Minimum detection diameter | 1 pixel |
| Minimum quantitative diameter | 3 pixels |
| Maximum diameter, voltage sweep | 200 pixels |
| Maximum diameter, flow sweep | $3d$ |
| Minimum circularity | 0.3 |
| Maximum aspect ratio | 2.0 |

The breakup regime was established for all experimental conditions. The Rayleigh regime is bounded below by the dripping-to-jetting transition near We ≈ 1 and above by the onset of wind-influenced breakup near We ≈ 40 (Lin and Reitz 1998). Most conditions satisfy We < 40, confirming that surface tension is the dominant restoring force and aerodynamic effects are modest. At the highest flow rate for water, $Q = 90\,\mathrm{mL/min}$, We approaches or exceeds this boundary. The weakening of acoustic influence observed at high velocities is therefore consistent with transition toward the wind-influenced regime.

## S1.5 Resolved-droplet region of interest, virtual gate, and image analysis

Resolved droplet statistics were measured from high-speed shadowgraph videos using a custom Python/OpenCV workflow. The droplet analysis was deliberately separated from the breakup-length analysis. Breakup length was measured from the connected jet, as described above, whereas droplet statistics were measured only from a downstream detached-droplet observation window. The connected jet core and long connected ligaments were excluded from the droplet region of interest (ROI) whenever possible, so the reported droplet population represents optically resolved detached objects crossing a prescribed gate, not all liquid structures visible in the full frame. The summary of the code's workflow is shown in Fig. S2.

The ROI protocol was fixed within each physical comparison. For the voltage sweep at $Q = 30\,\mathrm{mL/min}$, one ROI and one gate position were used for all voltages. For the Weber-number sweep, a different ROI was allowed for each flow rate because the jet trajectory and droplet cloud shifted with $Q$; however, for a given flow rate the identical ROI, threshold, and gate were used for the unforced and forced cases. For the fluid-property sweep, the same principle was applied within each fluid and drive comparison. This paired-ROI protocol avoids comparing a forced case and its control using different measurement windows.

The spatial calibration was

$$s = \frac{48\ \mathrm{mm}}{414\ \mathrm{pixels}} = 0.11594\ \mathrm{mm\ pixel^{-1}}. \tag{S11}$$

All droplet diameters are reported either as $D_{\mathrm{eq}}$ in millimetres or as the normalized value $D^*_{\mathrm{eq}} = D_{\mathrm{eq}}/d$, where $d = 1\,\mathrm{mm}$ is the nozzle diameter.

For each video, a bright background image was estimated from sampled frames using a high-percentile projection. Since droplets appeared as dark objects on a bright shadowgraph background, segmentation was performed using background-difference thresholding. The instantaneous grayscale frame was subtracted from the estimated background image, and pixels with an intensity difference greater than 50 grayscale levels were identified as candidate droplet pixels. This background-difference method was selected because it is less sensitive to nonuniform illumination than direct grayscale thresholding.

The final binary-threshold settings used for the analysis are summarized in Table S2. No image blurring was applied before thresholding because the droplet rims were sharply defined and additional smoothing could artificially merge neighboring droplets or alter their projected area. Morphological opening was not applied so that small resolved fragments were not removed. One iteration of morphological closing was applied to reconnect small gaps in the ring-like droplet rims commonly observed in shadowgraph images. The binary masks were then hole-filled before contour extraction, so that droplets were measured from the area enclosed by the outer contour rather than from only the dark rim pixels.

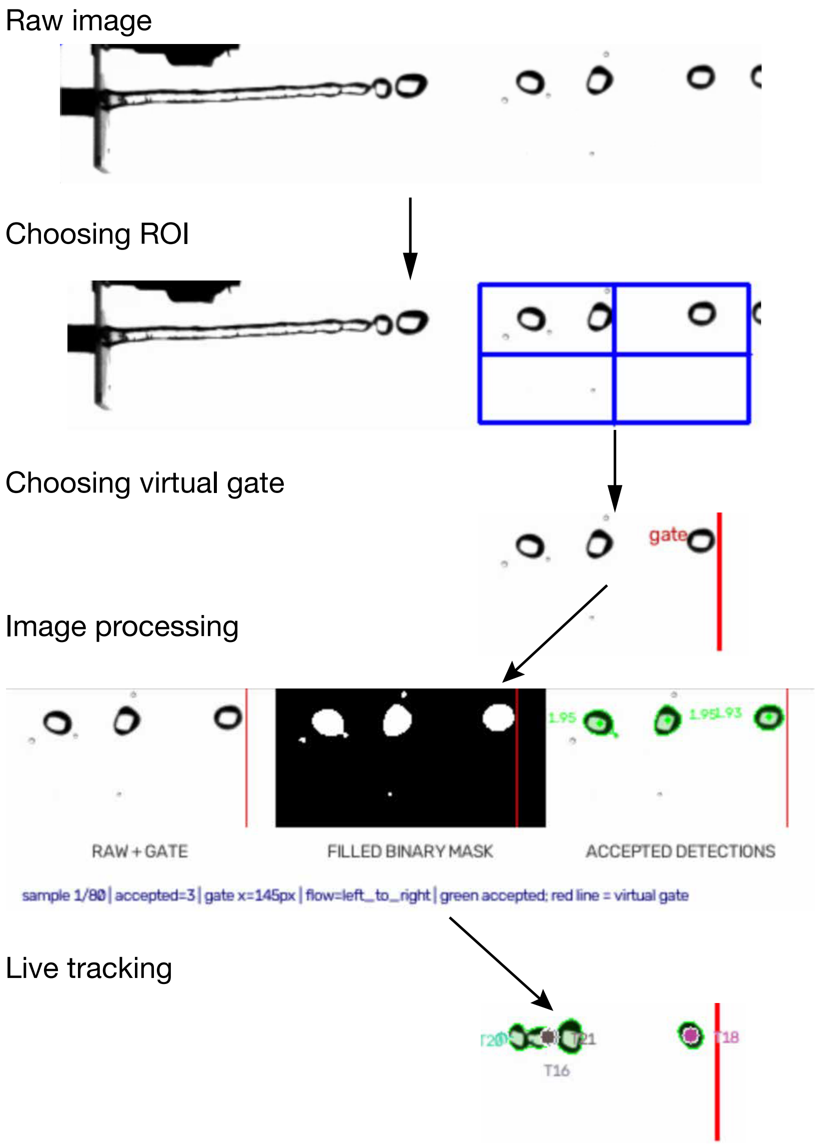


**Fig. S2** Representative ROI and virtual-gate workflow for resolved-droplet analysis. The full raw frame is shown only for orientation. The blue rectangle denotes the downstream ROI selected around detached droplets; the long connected jet and ligament are outside the processed droplet window. The red line is the virtual gate. The lower panels show the raw ROI with gate, the filled binary mask, the accepted detections after segmentation and filtering, and the live tracking visualization used for quality control. Each tracked droplet was counted once when its centroid crossed the virtual gate in the flow direction.

Droplet candidates were identified from the external contours of the filled binary mask. For each accepted contour, the projected equivalent diameter was calculated as

$$D_{\mathrm{eq}} = \sqrt{\frac{4A}{\pi}}\, s, \tag{S12}$$

where $A$ is the filled contour area in pixels squared. Thus, the reported diameter is the diameter of a circle with the same projected image area as the detected droplet.

Objects were filtered by size and shape before tracking. A one-pixel threshold was used only as an inclusive initial detection threshold so that small visible fragments were not discarded before tracking. Quantitative droplet-size statistics were then restricted to objects with $D_{\mathrm{eq}} \geq 3s \simeq 0.35\,\mathrm{mm}$, corresponding to at least three pixels across. This three-pixel cutoff is a conservative optical-resolution criterion and should not be interpreted as the lower physical limit of the spray; droplets smaller than this threshold were treated as unresolved. For the flow-rate sweep, an additional upper cutoff of $D^*_{\mathrm{eq}} \leq 3$ was used to remove obvious merged-blob artifacts. The circularity and aspect-ratio filters were used to reject strongly elongated structures, including connected ligament remnants, while retaining droplets that were moderately deformed or imperfectly circular in projection.

Droplets intersecting the ROI boundary were not automatically rejected. Because some valid droplets crossed near the edge of the selected measurement region, excluding all edge-touching droplets would bias the statistics toward droplets remaining fully centered inside the ROI. Edge-touching droplets were therefore flagged and their diameter was estimated using the available visible contour geometry through the edge-diameter estimation routine. These edge-based estimates were included only when the object otherwise satisfied the droplet size and shape criteria. Since edge-intersecting droplets are less certain than fully contained droplets, they were treated as a limitation of the image-based measurement. Videos were excluded from the final dataset when the jet or droplet cloud bent substantially out of the camera frame, because in those cases the ROI and virtual gate sampled only a partial and non-representative droplet population.

Accepted droplets were tracked by nearest-neighbor centroid matching to avoid repeated counting of the same object in consecutive high-speed frames. The tracking algorithm linked detections between adjacent frames using centroid position, with a maximum frame-to-frame linking distance and missed-frame allowance chosen to maintain tracks for rapidly moving droplets or temporarily incomplete masks. For left-to-right motion, a droplet was counted when a tracked centroid moved from $X < x_g$ to $X \geq x_g$ between adjacent frames. For the present videos this flow-direction criterion was equivalent to counting each detached droplet once at the downstream gate. Therefore, the reported droplet population represents resolved gate-crossing droplets rather than all segmented objects in all frames.

Live tracking visualization was used as a quality-control step during processing. The live display showed the filled detected droplets, active droplet tracks, and the virtual gate. This allowed visual confirmation that droplets were segmented, filled, tracked, and counted once at the gate. The live visualization was used to verify that the chosen ROI, threshold, and tracking parameters produced physically reasonable gate-crossing events.

Occasional merged droplets were still detected as single contours. These merged objects can overestimate the size of an individual droplet and mainly affect the upper tail of the diameter distribution. However, they were not expected to strongly skew the main reported trends because the same ROI, threshold, and tracking protocol was applied within each comparison group. In addition, the primary statistic $D_{50}$ is a median and is therefore relatively insensitive to a small number of large merged objects. The Sauter mean diameter $D_{32}$, which weights large droplets more strongly, was therefore interpreted with greater caution.

For each video, the droplet-size statistics were calculated from the set of gate-crossing droplet diameters. The reported quantities were the number-median diameter $D_{50}$ and the 25th and 75th percentile diameters. The interquartile range was reported using the 25th and 75th percentiles, $Q_{25}$ and $Q_{75}$.

# S2 Reduced-order correlation derivation for the water jet

The correlation is a compact representation of the water amplitude and velocity sweeps. The correlation combines the slow convective growth of the Rayleigh–Plateau instability with a thresholded acoustic capillary-wave branch that represents the effective disturbance generated near the wetted nozzle base.

## S2.1 Slow hydrodynamic subsystem

Let $R(z,t)$ denote the local jet radius and $U(z,t)$ the cross-section-averaged axial velocity. In the Rayleigh regime, a long-wave slender-jet approximation gives the leading mass and momentum balances

$$\partial_t(\pi R^2) + \partial_z(\pi R^2 U) = 0, \tag{S13}$$

$$\partial_t U + U\partial_z U = -\frac{\sigma}{\rho}\partial_z \kappa + 3\nu R^{-2}\partial_z\left(R^2\partial_z U\right), \tag{S14}$$

where $\nu = \mu/\rho$ and the curvature is approximated as $\kappa \approx R^{-1} - \partial_{zz}R$ for a slender axisymmetric interface. Gravity is not included explicitly in this local linear calculation because its leading effect in the present experiments is a slow downstream taper, which is more reliably absorbed into the measured no-ultrasound baseline than predicted from a local uniform-cylinder calculation.

Linearizing about a uniform base state $R = R_0$, $U = U_0$ with $R(z, t) = R_0+\eta(z, t)$ and $U(z, t) = U_0+u(z, t)$ gives

$$(\partial_t + U_0\partial_z)\eta = -\frac{R_0}{2}\partial_z u, \tag{S15}$$

$$(\partial_t + U_0\partial_z)u = \frac{\sigma}{\rho}\left(\frac{1}{R_0^2}\partial_z\eta + \partial_{zzz}\eta\right) + 3\nu\partial_{zz}u. \tag{S16}$$

Seeking modes proportional to $\exp(st + ikz)$ and defining $q = kR_0$ yields the viscous Rayleigh dispersion relation

$$s^2 + 3\nu k^2 s - \frac{\sigma}{2\rho R_0^3}q^2(1-q^2) = 0. \tag{S17}$$

Using the capillary time $\tau_\sigma = \sqrt{\rho R_0^3/\sigma}$, the dimensionless growth rate $\hat{s} = s\tau_\sigma$, and the radius-based Ohnesorge number $\mathrm{Oh}_R = \mu/\sqrt{\rho\sigma R_0}$, the positive root is

$$\hat{s}(q) = \frac{-3\mathrm{Oh}_R q^2 + \sqrt{9\mathrm{Oh}_R^2 q^4 + 2q^2(1-q^2)}}{2}. \tag{S18}$$

For water with $R_0 = 0.5\,\mathrm{mm}$ and the present material properties, this gives a fastest-growing mode close to the inviscid Rayleigh value. We denote the dimensional maximum growth rate by $s_{\max}$.

The amplitude $a(z)$ of the dominant slow capillary mode then grows approximately as

$$U_0\frac{da}{dz} = s_{\max}a, \qquad a(z) = a(0)\exp\left(\frac{s_{\max}z}{U_0}\right). \tag{S19}$$

If breakup occurs when this disturbance becomes $O(R_0)$, then the convective growth distance is

$$L_b = \frac{U_0}{s_{\max}}\ln\left(\frac{R_0}{a(0)}\right). \tag{S20}$$

This relation explains why the breakup length is sensitive to nozzle condition and wetting: those effects set the effective initial disturbance amplitude $a(0)$.

## S2.2 Fast acoustic subsystem and transmission into the jet

At 7 MHz, the acoustic wavelength in water is of order 0.2 mm, smaller than the nozzle diameter. The acoustic field therefore cannot be treated as cross-sectionally uniform. At leading order, the liquid acoustic field may be represented as a weakly compressible, irrotational perturbation,

$$\nabla^2\phi + \frac{\omega^2}{c^2}\phi = 0, \qquad \boldsymbol{u}_a = \nabla\phi e^{-i\omega t}, \qquad p_a = i\rho\omega\phi e^{-i\omega t}, \tag{S21}$$

where $\omega = 2\pi f$ and $c$ is the sound speed in the liquid. For a weakly tapered cylindrical jet, the first axisymmetric guided mode has the local form

$$\phi(r,z) \approx A_g(z)J_0\left(\alpha_1\frac{r}{R(z)}\right)\exp\left(i\int^z k_g(s)\,ds\right), \qquad k_g^2(z) = \frac{\omega^2}{c^2} - \frac{\alpha_1^2}{R^2(z)}, \tag{S22}$$

where $\alpha_1 = 2.4048$. The propagation condition $k_g^2 > 0$ gives the cutoff relation used in the main text. This justifies treating the actuation as a nozzle-coupled guided acoustic mode whose effective strength depends on the local jet radius and the mean state at the nozzle base.

The experiments show that the acoustic effect weakens as jet speed increases. A minimal representation is obtained by balancing the capillary pressure that maintains a stable wetted base, $p_\sigma \sim \sigma/d$, against the inertial dynamic pressure that strips or thins that base, $p_i \sim C_i\rho U_0^2$. This gives a rational transmission factor

$$T(\mathrm{We}) = \frac{p_\sigma}{p_\sigma + p_i} = \frac{1}{1+\mathrm{We}/\mathrm{We}_t}, \tag{S23}$$

where $\mathrm{We}_t = 1/C_i$ is an empirical scale for coupling loss at the wetted base.

## S2.3 Threshold capillary-wave branch

A smooth additive disturbance assumption, $a(0) = a_n + C\dot{\xi}_p^2$, would predict a continuous response from zero drive. The water data instead show a weak-response branch followed by a sudden decrease in breakup length. To represent this behavior, the correlation introduces an acoustically sustained capillary-wave amplitude $A_c$ that appears only when a reduced control parameter exceeds unity. The control parameter is

$$\Theta = \left(\frac{\dot{\xi}_p}{\dot{\xi}_c}\right)^2 T(\mathrm{We}) = \left(\frac{\dot{\xi}_p}{\dot{\xi}_c}\right)^2 \frac{1}{1 + \mathrm{We}/\mathrm{We}_t}. \tag{S24}$$

Here $\dot{\xi}_c$ is the critical transducer particle velocity needed to initiate the post-threshold acoustic capillary-wave branch.

The branch is represented by a Landau-type saturated amplitude equation,

$$\frac{dA_c}{dt} = \Gamma \frac{(\Theta - 1)_+}{\Theta_s + (\Theta - 1)_+} A_c - \beta A_c^3, \tag{S25}$$

where $(x)_+ = \max(x, 0)$, $\Gamma$ is a linear growth scale, $\beta > 0$ is a nonlinear saturation coefficient, and $\Theta_s$ determines the width of the post-onset transition. The steady finite-amplitude solution is

$$\frac{A_c}{R_0} = A_{\max} \left[\frac{\Theta - 1}{\Theta_s + \Theta - 1}\right]^{1/2} H(\Theta - 1), \tag{S26}$$

where $H$ is the Heaviside step function. This expression predicts no acoustic capillary-wave branch below onset, square-root growth just above onset, and saturation at large forcing.

The effective initial disturbance amplitude for the slow Rayleigh–Plateau growth is then the sum of a background contribution and the acoustically sustained capillary-wave amplitude,

$$a(0) = a_n(U_0) + A_c(\dot{\xi}_p, \mathrm{We}). \tag{S27}$$

Substitution into Eq. (S20) gives the closed reduced-order law

$$L_b(U_0, \dot{\xi}_p) = \frac{U_0}{s_{\max}} \ln \left[\frac{R_0}{a_n(U_0) + R_0 A_{\max} \left(\frac{\Theta - 1}{\Theta_s + \Theta - 1}\right)^{1/2} H(\Theta - 1)}\right]. \tag{S28}$$

The background amplitude $a_n(U_0)$ is obtained from the no-ultrasound baseline at the corresponding water condition,

$$a_n(U_0) = R_0 \exp\left[-\frac{s_{\max} L_{b,0}(U_0)}{U_0}\right]. \tag{S29}$$

This step is important because the experiments show campaign-to-campaign sensitivity to nozzle state and wetting. Using the no-ultrasound baseline prevents device-specific background differences from being incorrectly assigned to the acoustic threshold parameters.

## S2.4 Fitted parameters and interpretation

A joint fit to the water amplitude sweep and water velocity sweep gave $\dot{\xi}_c = 0.29\,\mathrm{m/s}$, $\mathrm{We}_t = 126$, $A_{\max} = 0.011$, $\Theta_s = 0.031$. For $R_0 = 0.5\,\mathrm{mm}$, the saturated acoustic capillary-wave amplitude is $R_0 A_{\max} \approx 5.5\,\mu\mathrm{m}$. The fit quality was $\chi^2/\mathrm{dof} = 1.46$. The correlation also gives a loss of effective acoustic shortening near $\mathrm{We} \approx 50$, consistent with the observed collapse of the forced and unforced water curves near $\mathrm{We} \approx 49$.

The correlation should be interpreted as follows. Below onset, acoustic energy may still modify the mean nozzle-base wetting state, but it does not produce a sustained capillary-wave branch strong enough to shorten the breakup length. Above onset, the acoustic branch increases the effective initial disturbance amplitude and therefore reduces the convective growth distance required to reach pinch-off. At high forcing, the branch saturates; additional input may be diverted into wetting, streaming, internal recirculation, satellite production, or competing interfacial modes.

## S2.5 Why the correlation is not applied to glycerol–water solutions

The glycerol–water solutions do not exhibit the same water-like weak-response branch followed by a sudden shortening. Instead, their breakup lengths decrease immediately at low forcing. Applying the water-threshold correlation to these fluids would therefore imply a shared onset mechanism that the data do not support. The immediate response suggests that viscous coupling near the wetted base changes how MHz forcing is converted into a low-frequency interfacial disturbance. Because only voltage sweeps were available for the viscous fluids, the acoustic threshold and saturated amplitude are also degenerate if the threshold form is forced onto the data. For these reasons, the glycerol–water solutions are discussed phenomenologically in the main text rather than compared to the reduced-order water correlation.

# References


Allen, M.P., Tildesley, D.J.: Computer Simulation of Liquids. Clarendon Press, Oxford (1989)

Bolstad, P.K., Frijlink, M., Hoff, L.: Evaluation of bonding techniques for ultrasound transducers. Microelectronics Reliability **151**, 115272 (2023) https://doi.org/10.1016/j.microrel.2023.115272

Benedict, L.H., Gould, R.D.: Towards better uncertainty estimates for turbulence statistics. Experiments in Fluids **22**, 129–136 (1996) https://doi.org/10.1007/s003480050030

Eggers, J., Villermaux, E.: Physics of liquid jets. Reports on Progress in Physics **71**(3), 036601 (2008) https://doi.org/10.1088/0034-4885/71/3/036601

Lin, S.P., Reitz, R.D.: Drop and spray formation from a liquid jet. Annual Review of Fluid Mechanics **30**, 85–105 (1998) https://doi.org/10.1146/annurev.fluid.30.1.85

McCarthy, M.J., Molloy, N.A.: Review of stability of liquid jets and the influence of nozzle design. The Chemical Engineering Journal **7**(1), 1–20 (1974) https://doi.org/10.1016/0300-9467(74)80021-3

Sciacchitano, A., Wieneke, B.: PIV uncertainty propagation. Measurement Science and Technology **27**(8), 084006 (2016) https://doi.org/10.1088/0957-0233/27/8/084006

Shilton, R., Yeo, L.Y., Friend, J.R.: Drilling Inlet and Outlet Ports in Brittle Substrates. Chips and Tips, Royal Society of Chemistry. Online technical note; accessed 2026-06-30 (2011). https://blogs.rsc.org/chipsandtips/2011/10/10/drilling-inlet-and-outlet-ports-in-brittle-substrates/

Takamura, K., Fischer, H., Morrow, N.R.: Physical properties of aqueous glycerol solutions. Journal of Petroleum Science and Engineering **98–99**, 50–60 (2012) https://doi.org/10.1016/j.petrol.2012.09.003

Vasan, A., Connacher, W., Friend, J.: Fabrication and characterization of thickness-mode piezoelectric devices for atomization and acoustofluidics. Journal of Visualized Experiments **162**, 61015 (2020) https://doi.org/10.3791/61015